

Role of Indian Ocean Dynamics on Accumulation of Buoyant Debris

Mirjam van der Mheen¹ , Charitha Pattiaratchi¹ , and Erik van Sebille² 

¹Oceans Graduate School and UWA Oceans Institute, University of Western Australia, Perth, Western Australia, Australia, ²Institute for Marine and Atmospheric Research Utrecht, Utrecht University, Utrecht, Netherlands

Key Points:

- The subtropical Indian Ocean garbage patch is very sensitive to different transport mechanisms
- Sensitivity to different transport mechanisms is likely a result of the unique Indian Ocean dynamics
- The surface Indian Ocean garbage patch is located to the west of the basin and is highly dispersive

Supporting Information:

- Supporting Information S1

Correspondence to:

M. van der Mheen,
mirjam.vandermheen@research.uwa.edu.au

Citation:

van der Mheen, M., Pattiaratchi, C., & van Sebille, E. (2019). Role of Indian Ocean dynamics on accumulation of buoyant debris. *Journal of Geophysical Research: Oceans*, 124, 2571–2590. <https://doi.org/10.1029/2018JC014806>

Received 25 NOV 2018

Accepted 20 MAR 2019

Accepted article online 28 MAR 2019

Published online 10 APR 2019

Abstract Buoyant marine plastic debris has become a serious problem affecting the marine environment. To fully understand the impact of this problem, it is important to understand the dynamics of buoyant debris in the ocean. Buoyant debris accumulates in “garbage patches” in each of the subtropical ocean basins because of Ekman convergence and associated downwelling at subtropical latitudes. However, the precise dynamics of the garbage patches are not well understood. This is especially true in the southern Indian Ocean (SIO), where observations are inconclusive about the existence and numerical models predict inconsistent locations of the SIO garbage patch. In addition, the oceanic and atmospheric dynamics in the SIO are very different from those in the other oceans. The aim of this paper is to determine the dynamics of the SIO garbage patch at different depths and under different transport mechanisms such as ocean surface currents, Stokes drift, and direct wind forcing. To achieve this, we use two types of ocean surface drifters as a proxy for buoyant debris. We derive transport matrices from observed drifter locations and simulate the global accumulation of buoyant debris. Our results indicate that the accumulation of buoyant debris in the SIO is much more sensitive to different transport mechanisms than in the other ocean basins. We relate this sensitivity to the unique oceanic and atmospheric dynamics of the SIO.

Plain Language Summary Plastic pollution of the oceans is a serious problem. To better understand how big the problem is, it is important to know how plastics move in the oceans and where they end up. Floating plastics move with ocean currents, waves, and wind. Because these interact with each other in complex ways, the exact movement of plastic in the ocean is hard to predict. From observations and computer simulations, it is known that plastic collects in subtropical “garbage patches” in the Pacific and Atlantic oceans, but it is not clear if this also happens in the Indian Ocean. The aim of this paper is to determine the different influences of ocean currents, waves, and wind on the development of a garbage patch in the Indian Ocean. Because we cannot track plastics, we use data from over 22,000 GPS-tracked drifting buoys that have been released worldwide in the oceans since 1979 to simulate the movement of plastic. Our results show that waves and wind prevent a garbage patch forming in the Indian Ocean. Because large amounts of plastic waste probably enter the Indian Ocean, an important question for follow-up research is what happens to these plastics if they do not collect in a garbage patch.

1. Introduction

Buoyant marine plastic debris (“plastics”) is a serious problem affecting the marine environment (Law, 2017). Because plastics do not degrade and are easily transported in the ocean, they can travel across entire ocean basins. As a result, plastic pollution is now a global problem, and plastics are found in the most remote locations on Earth (Barnes et al., 2010; C  zar et al., 2017; Duhec et al., 2015; Lavers & Bond, 2017). To fully understand the impact of this problem, as well as optimize mitigation and clean-up operations, it is important to understand the dynamics of plastics in the open ocean.

Plastics accumulate in so-called “garbage patches” in the subtropical ocean gyres. Moore et al. (2001) first observed a garbage patch in the North Pacific Ocean. Since then, several sampling studies have confirmed the existence of garbage patches in both the North Pacific and the North Atlantic oceans (Lebreton et al., 2018; van Sebille et al., 2015). There are fewer sampling studies in the Southern Hemisphere, but a sharp gradient in the measured plastic concentration suggests that there is a garbage patch in the South Pacific Ocean as well (Eriksen et al., 2013). In the South Atlantic and South Indian oceans, measurements are less conclusive about the existence of a garbage patch.

The accumulation mechanism of plastics in subtropical garbage patches can largely be explained by Ekman dynamics (Kubota, 1994; Kubota et al., 2005; Maximenko et al., 2012; van Sebille et al., 2012). Surface Ekman currents are driven by a combination of wind stress and the Coriolis force and converge at subtropical latitudes, between 20°N (°S) and 40°N (°S). Due to mass conservation, Ekman convergence results in an associated downwelling current. Because plastics remain at the ocean surface, they accumulate in these regions. So even though the ocean circulation is divergence-free in three dimensions, divergence and convergence of plastics can still occur in two dimensions.

According to Ekman dynamics, plastic accumulation should occur along the entire basin width in subtropical latitudes on both hemispheres. However, from observations and numerical modeling studies, it is clear that this is not the case. Several modeling studies (Kubota, 1994; Kubota et al., 2005; Lebreton et al., 2012; Martinez et al., 2009; Maximenko et al., 2012; van Sebille et al., 2012), using different numerical methods and assumptions, all show an increased accumulation of plastic toward the east of the subtropical North and South Pacific Ocean. This increased eastward accumulation is confirmed by measured plastic concentrations. In the North and South Atlantic Ocean, an increased accumulation slightly off-center toward the east occurs. To explain this, other mechanisms that may transport plastics need to be considered.

In addition to surface Ekman currents, plastics are also transported by geostrophic surface currents (Maximenko et al., 2009), which are driven by a combination of pressure gradients and the Coriolis force. Any buoyant object may also be transported by Stokes drift due to the nonlinearity of waves (Rohrs et al., 2012), as well as direct wind forcing or windage (e.g., Abascal et al., 2009; Breivik & Allen, 2008). An object's inertia may also influence its transport (Beron-Vera et al., 2016). How important each of these transport mechanisms is depends on the specific characteristics of the buoyant object (shape, size, and density; Breivik et al., 2011). The eventual path of an object drifting on the sea surface is determined by the combination and interaction of different transport mechanisms acting on different temporal and spatial scales.

Several theories try to explain the increased eastward accumulation of plastics in the subtropics. One of these theories suggests that plastic is advected eastward by geostrophic currents (Kubota, 1994; Kubota et al., 2005; Martinez et al., 2009). Another suggests that increased mesoscale eddy activity on the western side of the ocean basins disperses plastics (van Sebille et al., 2012), which counteracts the accumulation due to Ekman dynamics. At the moment, there is no consensus which of these theories is correct. This emphasizes that the understanding of the dynamics of the garbage patches is limited. This is especially true in the Indian Ocean (IO).

As mentioned previously, measurements of plastic concentrations are inconclusive regarding the existence of a subtropical garbage patch in the southern IO (SIO; between approximately [25,125]°E and [0,45]°S). In addition, results of numerical modeling studies predict inconsistent locations of a SIO garbage patch. Some model results show increased plastic concentrations in the center and toward the east of the SIO (Kubota et al., 2005; Lebreton et al., 2012; Maes et al., 2018), whereas others show an increase toward the west (Maximenko et al., 2012; van Sebille et al., 2012). Maes et al. (2018) recently also pointed out this inconsistency, but it has not yet been explained. Because several of the largest estimated coastal (Jambeck et al., 2015) and riverine (Lebreton et al., 2017; Schmidt et al., 2017) sources of plastics enter the IO, this is a relevant region to study. The atmospheric and oceanic dynamics of the IO differ significantly from the Pacific and Atlantic oceans (Schott et al., 2009), making it an interesting region to study for this reason as well.

The IO is bounded in the north by the Asian continent. Because of this, there is no northern subtropical gyre or garbage patch. Instead, the northern IO is dominated by the seasonally reversing monsoon system (Schott & McCreary, 2001). In the SIO, there is a wind-driven subtropical gyre similar to the other oceans (Stramma & Lutjeharms, 1997), but it has several unique features.

The South Indian Counter Current (SICC; see Figure 1b in Lambert et al., 2016) flows eastward through the center of the subtropical gyre, opposite to the direction expected from Sverdrup theory (Palastanga et al., 2007; Wijeratne et al., 2018). Subtropical countercurrents exist in the other oceans as well, but they dissolve halfway through the basin. The SICC flows across the entire width of the SIO and splits into three separate branches between the southern tip of Madagascar and the western coast of Australia (Lambert et al., 2016; Menezes et al., 2014). The SICC is also associated with high activity of westward propagating eddies (Dilmahamod et al., 2018).

The eastern and western boundaries of the SIO subtropical gyre also have unique features. In contrast to all other eastern boundary currents, the Leeuwin Current flows poleward and is driven by an alongshore pressure gradient rather than wind (Pattiaratchi & Woo, 2009). The eastern boundary also has larger eddy activity than any other eastern boundary region (Jian & Wu, 2011). At the western boundary, the Agulhas Current flows poleward and continues to flow poleward after the African coastline terminates around 35°S (Beal et al., 2011; Lutjeharms, 2006). This provides a connection between the SIO and South Atlantic Ocean.

The aim of this paper is to determine the influence of different transport mechanisms on the dynamics of the subtropical SIO garbage patch. To do this, we use ocean surface drifters as a proxy for plastics. However, the drifters may be equally valid proxies for other types of buoyant objects, so from now on we refer to “buoyant debris” rather than plastics. Similarly, we refer to “accumulation regions” instead of garbage patches, because garbage patches are mostly associated with plastics.

We simulate the accumulation of buoyant debris using transport matrices based on observed drifter locations, which we explain in detail in section 2.2. This method has previously been used to simulate the evolution and dynamics of subtropical accumulation regions (Maximenko et al., 2012; van Sebille et al., 2012). Different from previous studies, we distinguish between two types of drifters: drogued and undrogued drifters. Drogued drifters are transported by ocean currents at a nominal 15-m depth (Niiler et al., 1995). Undrogued drifters are transported by ocean currents in the uppermost surface layer (0- to 1-m depth) as well as Stokes drift and windage (Poulain et al., 2009). By distinguishing between these two types of drifters and creating two separate transport matrices, we can determine the influence of different transport mechanisms on the dynamics of the SIO accumulation region.

Our results indicate that accumulation of buoyant debris in the SIO is much more sensitive to different transport mechanisms than the other oceans. We relate this to the unique dynamics of the IO.

2. Data Sets and Methods

2.1. Global Drifter Data Sets: Drogued and Undrogued

We use observed drifter locations from Surface Velocity Program drifters (Lumpkin & Pazos, 2007) deployed in the National Oceanic and Atmospheric Administration Global Drifter Program. Data from 22,602 drifters from 1979 until February 2018 are currently available. The drifters transmit their locations through satellite several times a day. After quality control the locations are interpolated and made available by the National Oceanic and Atmospheric Administration at 6-hourly intervals (Hansen & Poulain, 1996). Depending on the position of the Argos or Global Positioning System satellites, drifter locations are accurate within 15-m to 1-km (Lumpkin & Pazos, 2007). These errors are negligible for transport between 1° grid cells (see section 2.2) that we are interested in here (McAdam & van Sebille, 2018). The spatial coverage of the drifters spans most of the global oceans (Figure 1a).

The drifters are made out of a spherical surface float with a ~30- to 40-cm diameter, with a “holey-sock” drogue attached to it (Lumpkin & Pazos, 2007). The drogue is cylindrical with a ~60- to 90-cm diameter and ~6 m long. The drogue is centered at 15-m depth. Its purpose is to ensure that drogued drifters follow the ocean currents at a nominal 15-m depth by minimizing wind slip (Niiler et al., 1995).

Because of constant flexing, the buoy-drogue connection is vulnerable to mechanical failure and all drifters lose their drogue at some point in their lifetime. Undrogued drifters are transported by ocean currents in the uppermost surface layer as well as Stokes drift and windage (Poulain et al., 2009). A sensor on the surface float detects when the drogue is lost, so drogued and undrogued drifters can be distinguished from each other. However, several studies indicate that the sensor does not always detect drogue loss correctly (e.g., Grodsky et al., 2011). Lumpkin et al. (2013) therefore analyzed and corrected the full drifter data set for drogue presence based on drifter velocities. We use the corrected data set here.

We use separate data sets of drogued and undrogued drifters. Approximately 45% of all observed locations come from drogued drifters (15,940,545 locations from 22,602 individual drifters), versus 55% from undrogued drifters (19,407,024 locations from 22,602 individual drifters). These locations are spread unevenly across the global oceans (Figures 1c and 1e), due to both the uneven deployment (drogued drifters, Figure 1b) or drogue loss (undrogued drifters, Figure 1d), as well as advection of the drifters.

We are interested in the effect of advection on the distribution of drogued and undrogued drifters, independent of the drifter release, drogue loss, or death locations (Figure 1f). In addition, we want to study long-term

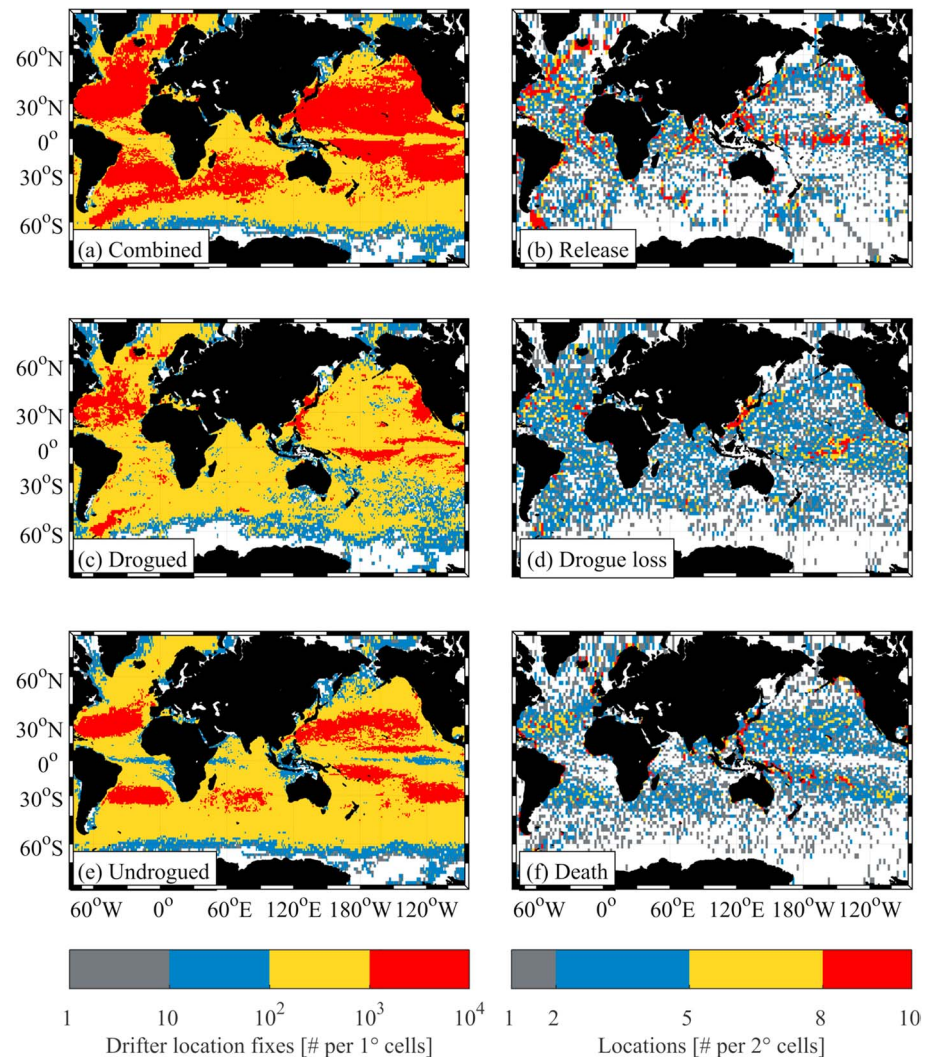


Figure 1. Number of observed drifter location fixes from the National Oceanic and Atmospheric Administration's Global Drifter Program between 1979 and February 2018 per $1 \times 1^\circ$ cells for (a) combined data set of drogued and undrogued drifters, (c) drogued drifters, and (e) undrogued drifters. Number of (b) release, (d) drogue loss, and (f) death locations of drifters between 1979 and February 2018 per $2 \times 2^\circ$ cells. White signifies areas with no observed drifter locations.

accumulation patterns (i.e., 50 years; see section 2.2) of drogued and undrogued drifters, but the average lifetime of an individual drifter is only ~ 1 year (this includes drifters that beach or are picked up by boats while they are still transmitting, different from the lifetime analysis by Lumpkin & Pazos, 2007). We eliminate the effect of drifter deployment locations (Maximenko et al., 2012) and simulate transport and accumulation on much longer timescales than the lifetime of a drifter (van Sebille et al., 2012) by creating transport matrices from observed drifter locations.

2.2. Transport Matrices

A range of oceanographic studies have used transport matrices to capture regional and global scale ocean dynamics (e.g., C  zar et al., 2017; Dellnitz et al., 2009; Khatiwala et al., 2005; Maximenko et al., 2012; Miron et al., 2019; Sherman & van Sebille, 2016; van Sebille et al., 2012). More specifically, van Sebille et al. (2015) compared global particle tracking simulations forced by a hydrodynamic model by Lebreton et al. (2012) to drifter transport matrix simulations by Maximenko et al. (2012). On the basin scale the results were similar and the drifter transport matrix method is therefore considered adequate to represent the large spatial and temporal scale transport (McAdam & van Sebille, 2018).

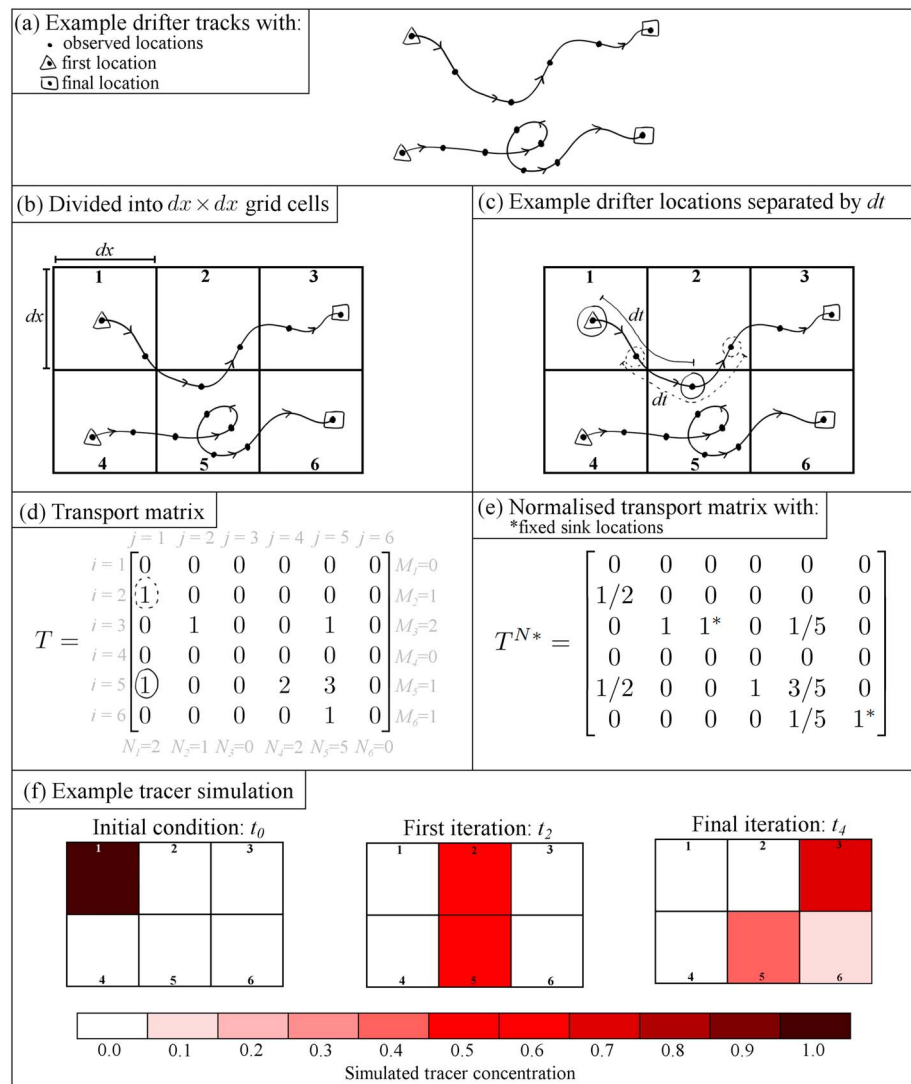


Figure 2. Example of how to construct a transport matrix from observed drifter locations and run tracer simulations. (a) Example tracks and observed locations of two drifters. (b) Area divided into $n = 6$ grid cells of size $dx \times dx$, the first step to create a transport matrix. (c) Example of the drifter locations at time $t_0, t_0 + dt, t_1$, and $t_1 + dt$. The solid and dashed circles indicate how these locations are used to fill the transport matrix shown in panel d. (d) The transport matrix T . The columns j of T indicate the grid cell that a drifter is in at a time t , and the rows i the grid cell that a drifter is in at time $t + dt$. The sum of each column $N_j = \sum_{i=1}^n T_{i,j}$ and each row $M_i = \sum_{j=1}^n T_{i,j}$ is also shown. N_j represents the total number of observed locations that have left a grid cell, M_i the total number that has entered. (e) The normalized transport matrix with fixed sink locations in grid cells 3 and 6 to prevent tracer from disappearing during a simulation. (f) Example tracer simulation of 4 days, assuming that $dt = 2$ days, and starting with tracer in grid cell 1. The simulation illustrates how the transport matrix diffuses tracer across grid cells depending on the number of observed drifter locations.

Several studies describe the construction of transport matrices (e.g., Cózar et al., 2017; Froyland et al., 2014; Khatiwala et al., 2005; McAdam & van Sebille, 2018; Maximenko et al., 2012; Ser-Giacomi et al., 2015; Sherman & van Sebille, 2016; van Sebille et al., 2012). Maximenko et al. (2012) give a mathematical description of the construction of a transport matrix from observed drifter locations. McAdam and van Sebille (2018) give a descriptive overview. We explain step by step how to construct a transport matrix and run tracer simulations using an example.

2.2.1. An Example

Say that we have two drifters with observed locations as shown in Figure 2a. To construct a transport matrix, we first divide the ocean into grid cells of size $dx \times dx$ (Figure 2b). We end up with a total of $n = 6$ grid cells,

which we label successively. The transport matrix T is an $n \times n$ matrix, which we fill using the following method.

We take a drifter's location \vec{x} at a certain time t , and the drifter's location a "separation time" dt later. Let us say that observed locations are returned at 1-day intervals by the example drifters, and set $dt = 2$ days. The columns j of T represent the grid cell that a drifter is in at a time t , the rows i of T the grid cell that a drifter is in at a time $t + dt$. For the upper drifter track, $\vec{x}(t_0)$ is in grid cell 1, so column $j = 1$ in T , and $\vec{x}(t_0 + dt)$ is in grid cell 5, so row $i = 5$ in T (Figure 2c). In the transport matrix, we therefore note $T_{5,1} = 1$. We do this for all observed locations for all drifters to get the transport matrix T in Figure 2d.

Before we can use T to run tracer simulations, we need to normalize it. The sum of a column j of T , $N_j = \sum_{i=1}^n T_{i,j}$ represents the total number of observed locations that have left a grid cell. To prevent tracer from being created during a simulation, we normalize T by dividing all columns $T_{*,j}$ by N_j . So the normalized transport matrix

$$T^N = \frac{T_{*,j}}{N_j} \text{ for } j = [1, n], \text{ if } N_j \neq 0. \quad (1)$$

Grid cells 3 and 6 are sink locations: drifters have entered these grid cells but never left. We will discuss how we handle sink locations in the transport matrices based on global drifter data sets in section 2.2.2. For now, we want to run a tracer simulation and we do not want the tracer to disappear from this simulation, so we set $T_{3,3}^N = 1$ and $T_{6,6}^N = 1$. The normalized transport matrix with these adjusted "fixed" sink locations T^{N*} is shown in Figure 2e.

The transport matrix can be interpreted as a set of probability density functions for each grid cell. So the transport matrix gives the probability that a drifter entering a grid cell j will move into any other grid cell within a time dt . Because drifters mostly move into a limited number of neighboring grid cells, the transport matrix is very sparse. When we run a tracer simulation, we divide tracer over grid cells based on the probabilities contained in the transport matrix. We will illustrate how this works by running a simple simulation with the T^{N*} .

Let us start the simulation with a tracer concentration of 1 in grid cell 1. We store tracer in a vector \vec{R} , so the initial condition is given by $\vec{R}_{t_0} = [1 \ 0 \ 0 \ 0 \ 0 \ 0]^T$, where the superscript T indicates the transpose of the vector. To simulate tracer advection, we multiply T^{N*} with \vec{R}_{t_0} . This gives us the tracer concentration at time $t_0 + dt$, where dt is the separation time that we used earlier to construct the transport matrix:

$$\vec{R}_{t_0+dt} = T^{N*} \cdot \vec{R}_{t_0}. \quad (2)$$

If we want to run a simulation for a total time of t_{total} , we need to repeat this multiplication t_{total}/dt times. Let us set $t_{\text{total}} = 4$ days, so we run two iterations. Running this simulation results in the tracer concentration in Figure 2f.

2.2.2. Transport Matrices From Global Drifter Data Sets

To create transport matrices from global drifter data sets and run tracer simulations, we use the same methodology as described in section 2.2.1. Sink locations in the transport matrix T can be handled in different ways. We can ensure that tracer remains in sinks forever ("fixed sink locations"), as we did in the example, or we can remove sink locations from T completely. For the transport matrices based on global drifter data sets, we remove sinks completely for two reasons. First, sink locations in T not only represent actual sinks (e.g., drifters beached) but also virtual sinks (e.g., drifters ran out of battery). Second, the sinks in T are not all-inclusive because relatively few drifters move along coastlines or enter the Southern and Arctic oceans, where most sinks in T are located (supporting information Figure S1).

To determine the influence of our chosen sink handling method on the simulation results, we performed a sensitivity analysis using transport matrices with both fixed sink locations and with sink locations removed. Although the simulation results are somewhat sensitive to the chosen sink handling method (supporting information Figure S2), this does not change our main results and conclusions. We therefore remove sinks from T for the reasons mentioned above. We find sink locations using the following method.

As defined earlier, the sum of a column j of T , $N_j = \sum_{i=1}^n T_{i,j}$ represents the total number of observed locations that have left grid cell j . Similarly, the sum of a row i of T , $M_i = \sum_{j=1}^n T_{i,j}$ represents the total

number of observed locations that have entered grid cell i . In the simplest case, a sink is a grid cell k that drifters have entered ($M_k \neq 0$) but never left ($N_k = 0$). This was the case for grid cells 3 and 6 in the example in section 2.2.1. However, drifters can also have several observed locations in a sink grid cell, in which case $N_k \neq 0$. We can still recognize this location as a sink in T because the only observed locations “leaving” this grid cell enter straight back into it. This means that for these sink locations $N_k = T_{k,k}$. This condition is also satisfied if $N_k = 0$, so we find that sinks are grid cells k that satisfy the condition

$$N_k = T_{k,k} \ \& \ M_k \neq 0, \quad (3)$$

where we add the condition $M_k \neq 0$ to exclude grid cells that do not contain any observed locations at all.

Next, we remove sinks from T by setting the entire row k in the transport matrix to 0, $T_{*,k} = 0$. This ensures that no tracer enters the sink locations k . Removing a sink location often only shifts the sink to a neighboring grid cell. We therefore remove sinks iteratively until there are no more grid cells left in T that satisfy condition (3). After removing all sinks, we normalize T according to equation (1) and run simulations by iterating the matrix multiplication (2).

Following van Sebille et al. (2012), we use $dx = 1^\circ$ and $dt = 60$ days to construct transport matrices from global drifter data sets. The simulation results are sensitive to the choice of dx and dt , which we discuss further in section 2.2.3. We construct three different transport matrices: (1) A “combined transport matrix” based on locations from drogued and undrogued drifters combined, which we use to run “combined simulations.” We run combined simulations for comparison with previous studies. (2) A “drogued transport matrix” based on locations from drogued drifters only, with which we run “drogued simulations.” We expect the drogued simulations to represent the ocean dynamics at a nominal 15-m depth. (3) An “undrogued transport matrix” based on locations from undrogued drifters only, with which we run “undrogued simulations.” We expect the undrogued simulations to represent ocean surface dynamics, which includes the uppermost surface currents as well as Stokes drift and windage.

We run 50-year simulations starting from a uniform initial condition with tracer spread evenly across the global oceans (tracer concentration = 1 per $1 \times 1^\circ$ grid cell). After 50 years, the amount of tracer in the subtropical accumulation regions converges to stationary solutions. The uniform initial condition is not a realistic representation of plastic sources, but we choose it deliberately because we are interested in the dynamics of buoyant debris independent of the distribution of sources. In other words, we choose this uniform condition so that we know that our results are due to dynamics and not influenced by the distribution of sources in a specific region. The same approach has been used by Maximenko et al. (2012) and McAdam and van Sebille (2018). In section 4 we discuss the likely implications if we do take plastic sources into account.

Following van Sebille et al. (2012), we define accumulation regions as connected regions where the concentration of tracer in an accumulation region is at least 2 times larger than if the tracer is distributed evenly across the global oceans, so tracer concentration > 2 per $1 \times 1^\circ$ grid cell. We add the condition that accumulation regions should contain at least 50 adjacent grid cells, to capture relatively large accumulation regions.

2.2.3. Advantages and Limitations of the Transport Matrix Method

There are several advantages and limitations to the drifter transport matrix method. The main advantage is that the transport matrix captures the statistics of the movement of actual drifting objects without the need for us to understand the physics behind their movement. This is important because, although we can make rough estimates about the relative importance of different transport mechanisms that influence drifting objects (e.g., Abascal et al., 2009; Breivik & Allen, 2008; Poulain et al., 2009), their actual behavior is too complex for a model to describe (Maximenko et al., 2012).

The main limitation of the drifter transport matrix method is that the quality of the transport matrices depends on the available drifter trajectories (McAdam & van Sebille, 2018), both spatially and temporally. Spatially, some areas of the Southern and Arctic oceans, as well as the Indonesian Throughflow have orders of magnitude fewer, or even 0, observed drifter locations than the subtropical ocean basins (Figures 1a, 1c, and 1e). These are important regions of exchange between oceans and the relative undersampling of these regions is a limitation of the drifter transport matrix method. However, the subtropical ocean basins contain between $\mathcal{O}(10^2)$ and $\mathcal{O}(10^4)$ drifter locations per 1° grid cells, which is sufficient to represent the dynamics of the subtropical accumulation regions that we are interested in (e.g., Cózar et al., 2017; Maximenko et al., 2012; McAdam & van Sebille, 2018; Sherman & van Sebille, 2016).

The number of drifters transmitting their location at a specific time is limited. For example, on 28 February 2018 there were 1,376 active drifters. Using only these drifter trajectories would give us insufficient data to construct a transport matrix. To solve this problem, we assume statistical stationarity of the underlying flow field (Maximenko et al., 2012). In other words, we construct a single transport matrix using all observed drifter locations between 1979 until February 2018. Because ocean currents show variability on different time scales, this assumption is not strictly valid. However, this does not mean that temporal variations are unaccounted for in the transport matrix. Instead, variability is present in the transport matrix as diffusion (Maximenko et al., 2012), which allows simulated tracer to take multiple paths. So the transport matrix represents the ocean surface circulation from 1979 to 2018 (the current time span of the global drifter data set) including all temporal variations sampled by the drifters. This means that although the transport matrix cannot be used to simulate transport of buoyant debris for a specific time period (i.e., a specific day, month, or year), it adequately represents the dynamics of large-scale and long-term transport (e.g., Cózar et al., 2017; Maximenko et al., 2012; McAdam & van Sebille, 2018; Sherman & van Sebille, 2016).

The number of observed drifter locations with which we construct transport matrices varies over the years (supporting information Figure S5, top panels). This might raise concern that the transport matrices are biased toward a specific season or mode of climate variability. However, the number of observed drogued and undrogued drifter locations is distributed very uniformly over each month (supporting information Figure S5, middle panels). In addition, the number of drifter locations as a function of, for example, the Multivariate El Niño Southern Oscillation Index (Wolter & Timlin, 1993, 1998), matches the occurrence of the Multivariate El Niño Southern Oscillation Index values between 1979 and 2018 very well (supporting information Figure S5, bottom panels). It is therefore unlikely that the drifter transport matrices we derive here are biased toward a specific season or mode of climate variability.

It is also possible to create multiple transport matrices from the global drifter data set that, for example, represent different seasons. This was done by van Sebille et al. (2012): They created six separate transport matrices that each represented 2 months. They then ran simulations by alternating the six transport matrices, which allowed them to include the seasonal cycle in their simulations. Unfortunately, separating the global drifter data set into drogued and undrogued data sets and then into seasons leaves us with insufficient drifter locations to construct transport matrices. We therefore use a single transport matrix that contains all seasons, similar to, for example, Lumpkin et al. (2016) and Maximenko et al. (2012). However, we did perform a sensitivity analysis using the combined drifter data set to determine the influence of including the seasonal cycle (supporting information Figure S6). Although the simulation results are sensitive to included seasonality, the general long-term (i.e., 50 years) behavior of the subtropical accumulation regions does not change and including seasonality is therefore unlikely to significantly alter our main results and conclusions.

Finally, to construct transport matrices, we use grid cells of finite size dx and finite separation time dt . It is important to note that dx and dt that we use to construct transport matrices cannot be interpreted in the same way as the grid resolution and time step of a primitive-equation ocean circulation model (McAdam & van Sebille, 2018). The drifters are advected by the full flow field, including submesoscale turbulence. As a result, these effects are present in the observed drifter locations that we use to construct transport matrices, regardless of the grid cell size dx and separation time dt . However, the discretization into grid cells of finite size dx and a finite separation time dt can lead to artificial dispersion in the transport matrix (Maximenko et al., 2012; McAdam & van Sebille, 2018). The reasons for this are explained in detail by McAdam and van Sebille (2018). As a consequence, the simulation results are sensitive to the choice of dx and dt . We repeated sensitivity analyses performed by McAdam and van Sebille (2018; supporting information Figures S3 and S4). In general, the drogued and undrogued simulations are more sensitive to different values of dx and dt than the combined simulations. This sensitivity does not change our main results and conclusions.

To summarize, the quality of drifter transport matrices is limited by the number of available drifter trajectories. By assuming statistical stationarity of the underlying flow field, we can use all observed drifter locations between 1979 and 2018 to construct transport matrices. These transport matrices are considered to adequately represent the large-scale and long-term transport of buoyant debris that we are interested in here (e.g., Cózar et al., 2017; Maximenko et al., 2012; McAdam & van Sebille, 2018; Sherman & van Sebille, 2016). By using transport matrices derived from observed drogued and undrogued drifter locations, we can simulate the effect of different transport mechanisms on accumulation patterns of actual drifting objects. As

a next step, we can then determine which transport mechanisms are responsible and simulate these using more conventional particle tracking models.

2.3. Global Wind and Current Fields

We use global wind and current fields from 1 January 1993 until 31 December 2015 for several purposes in this study. We obtain daily wind fields at 10-m height interpolated to $0.5 \times 0.5^\circ$ horizontal resolution from the European Centre for Medium-Range Weather Forecasts ERA-Interim Reanalysis product (Dee et al., 2011). From the GlobCurrent-v3 product (Rio et al., 2014) we get daily geostrophic, Ekman surface, and 15-m depth current fields with a $0.25 \times 0.25^\circ$ horizontal resolution, and daily Stokes drift data with a $0.5 \times 0.5^\circ$ horizontal resolution. We use the daily wind and current fields as a forcing for particle tracking simulations (see section 2.4). We also calculate global mean fields.

The 15-m depth Ekman currents are derived from satellite altimetry data and velocities of drogued drifters. This data set is therefore not fully independent from the drogued drifter data set. Because this is the only data available of 15-m depth Ekman currents, we still continue to use it.

Following Martinez et al. (2009), we calculate the global mean geostrophic component of the eddy kinetic energy as

$$EKE_g = \overline{0.5 \cdot [(u_g - \bar{u}_g)^2 + (v_g - \bar{v}_g)^2]}, \quad (4)$$

where the overline denotes the temporal mean and u_g and v_g are daily, and \bar{u}_g and \bar{v}_g are mean geostrophic currents between 1993 and 2015 in the zonal and meridional directions, respectively.

2.4. Particle Tracking Simulations

To confirm the results from the drifter transport matrix simulations, we run additional simulations forced by two different forcing fields: (1) a forcing field that likely transports drogued drifters, consisting of geostrophic currents and Ekman 15-m depth currents, the “ $\bar{u}_g + \bar{u}_{E15m}$ simulation”; (2) a forcing field that likely transports undrogued drifters, consisting of geostrophic currents, Ekman surface currents, Stokes drift, and 1% windage, the “ $\bar{u}_g + \bar{u}_{E0m} + \bar{u}_{St} + 0.01 \cdot \bar{u}_{10}$ simulation.” Windage is calculated as 1% of the wind field at 10-m height; a value of 1% was suggested for the undrogued drifters by Poulain et al. (2009). We use both daily forcing fields from 1 January 1993 until 31 December 2015 and global mean forcing fields described in section 2.3 to force these simulations. In section 3.3 we explain why we use global mean forcing fields in addition to the temporally varying fields.

We run Lagrangian particle tracking simulations and use the virtual particle trajectories to create transport matrices (e.g., Froyland et al., 2014; Khatiwala et al., 2005; Ser-Giacomi et al., 2015), in the same way as from observed drifter locations. Next, we run 50-year tracer simulations starting from a uniform initial condition. We do this, instead of running 50-year particle tracking simulations, because the comparison with the drifter transport matrix simulations is more straightforward.

We use the OceanParcels Lagrangian analysis toolkit (Lange & van Sebille, 2017) to run global particle tracking simulations. We interpolate all forcing fields to $0.5 \times 0.5^\circ$ horizontal resolution. In the simulations using temporally varying fields, we release one particle in each grid cell. We reset the particle location every 60 days (e.g., Froyland et al., 2014; Khatiwala et al., 2005), which results in 140 simulations between 1 January 1993 and 31 December 2015. In the simulations using global mean fields, we release 100 particles in each grid cell. Because in this case we use stationary global mean forcing fields, we only need to run a particle tracking simulation of 60 days (Khatiwala et al., 2005). This results in roughly 20 million virtual locations in the temporally varying simulations, and 15 million virtual locations in the global mean simulations to construct a transport matrix: the same order of magnitude as the number of observed drifter locations available for the drogued and undrogued transport matrices. To construct the transport matrices, we use a grid size $dx = 1^\circ$ and a separation time $dt = 60$ days.

We force the particle tracking simulations with fields from 1993 until 2015 and compare these simulations with the drogued and undrogued drifter transport matrix simulations. The drifter transport matrices are based on drifter data from 1979 until 2018. To confirm that we can make this comparison, we also ran drifter transport matrix simulations based only on drifter locations observed between 1993 and 2015 (supporting information Figure S7). There are only minor differences between the two simulations that do not influence our main results and conclusions, so we go ahead and compare the results of the full drifter transport matrix

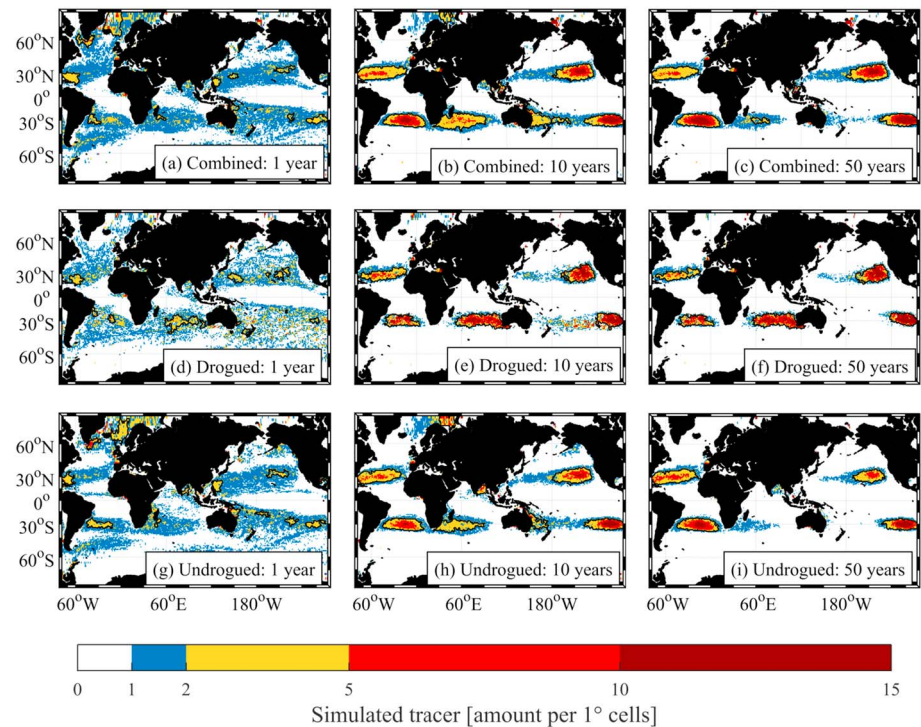


Figure 3. Simulated tracer concentration and locations of the five subtropical accumulation regions using transport matrices derived from (a, b, c) combined drogued and undrogued drifter locations, (d, e, f) drogued drifter locations, and (g, h, i) undrogued drifter locations. The simulated tracer density starting from a uniform initial condition is shown after (a, d, g) 1 year, (b, e, h) 10 years, and (c, f, i) 50 years. Black lines indicate the spatial extent of the subtropical accumulation regions, defined as regions with at least 50 adjacent grid cells where the tracer concentration exceeds $2 \text{ per } 1^\circ \times 1^\circ \text{ cell}$.

simulations (from data between 1979 and 2018) with the particle tracking simulations forced with current and wind fields between 1993 and 2015.

3. Results

3.1. Drifter Transport Matrix Simulations

We use the combined, drogued, and undrogued transport matrices to simulate the accumulation of buoyant debris over a period of 50 years, starting from a uniform initial condition with tracer spread evenly across the global oceans. In all three simulations (Figure 3), tracer quickly depletes from the equator and converges in the subtropics after 1 year of simulation, as we expect due to Ekman transport. After 10 years, large-scale subtropical accumulation regions form in all simulations. After 50 years the accumulation regions in the Pacific and Atlantic oceans are still present in all simulations and have condensed or increased in tracer concentration. In the IO accumulation region, the tracer concentration has decreased significantly in the combined and undrogued simulations.

Our combined simulation is set up using the same methodology as Maximenko et al. (2012). The only difference is that we have roughly twice as many drifters available to construct our transport matrix. We therefore expect the results of the combined simulation (Figures 3a and 3b) to be very similar to those of Maximenko et al. (2012), which they are. The exception is that in our simulation an accumulation region forms in the Barents Sea. This accumulation has previously been noted in simulations by van Sebille et al. (2012) and has since been confirmed by sampling studies (Cózar et al., 2017).

We are interested in comparing the drogued and undrogued simulations because they illustrate the large-scale and long-term effect of different transport mechanisms on the accumulation of buoyant debris. After 50 years, the subtropical accumulation regions in the drogued (Figure 3f) and undrogued (Figure 3i) simulations are relatively similar in the Pacific and Atlantic oceans. Although the accumulation regions vary in shape and concentration between the simulations, their general location is remarkably robust. This

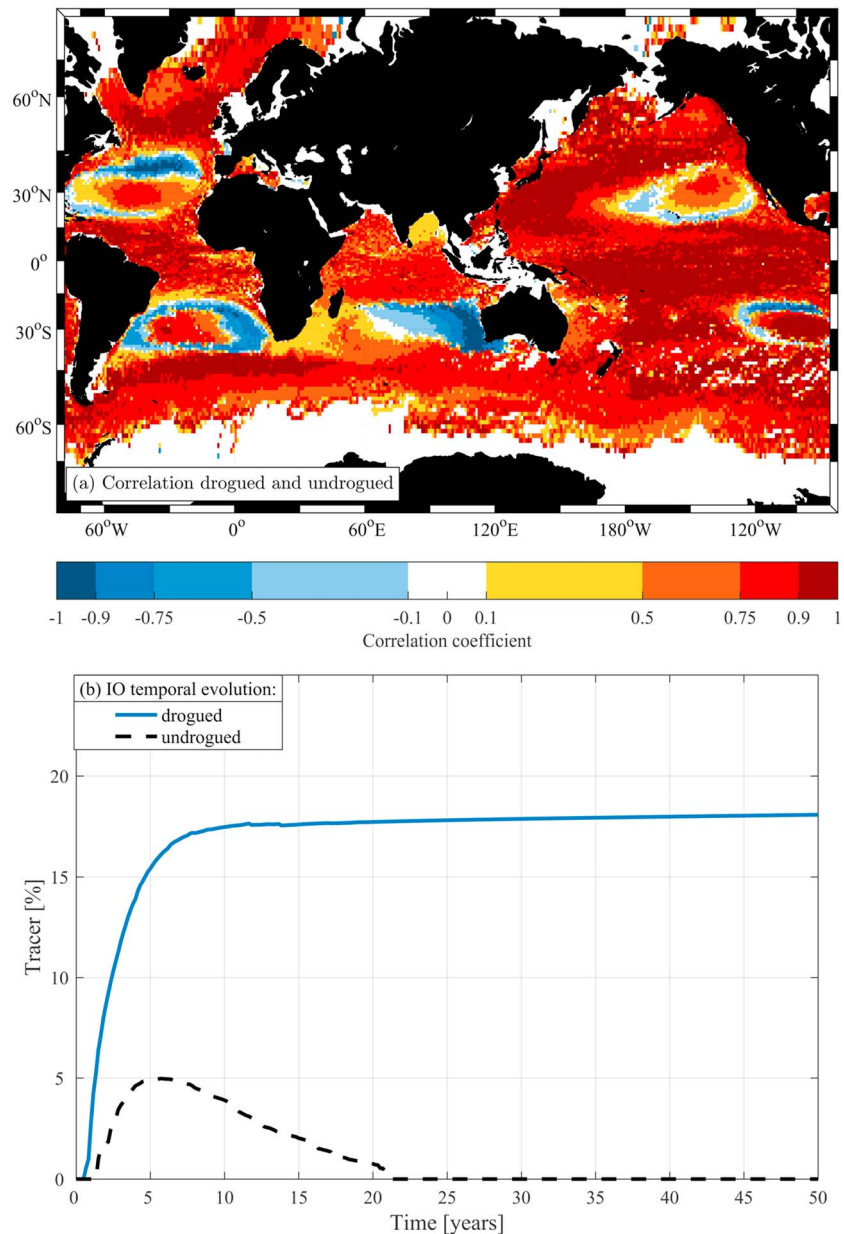


Figure 4. (a) Point-wise linear Pearson correlation coefficient in each grid cell between simulations using transport matrices derived from drogued and undrogued drifter locations, calculated over a simulation time of 50 years (i.e., 300 two-month values). A correlation value of 1 indicates perfect correlation; -1 indicates perfect anticorrelation. Correlations that are not statistically significant (within a confidence interval of 95%) are omitted (in white). (b) Temporal evolution of the size of the subtropical southern Indian Ocean accumulation region over 50 years of simulation using the transport matrices based on drogued and undrogued drifter locations. The accumulation size is defined as a region with at least 50 adjacent grid cells where the tracer concentration exceeds 2 per $1^\circ \times 1^\circ$ cell (e.g., black lines in Figure 3). Tracer is given as a percentage of the total amount of globally available tracer in the simulation.

is confirmed by the strong statistically significant correlation between the drogued and undrogued simulations in the center of the accumulation regions in the Pacific and Atlantic oceans in Figure 4a. In the SIO, the differences are a lot more pronounced.

The SIO subtropical accumulation region in the drogued simulation (“drogued SIO accumulation”) has a high concentration of tracer, is centered slightly toward the east, and spans almost the entire basin width of the SIO (Figures 3e and 3f; between 55–126°E and 20–39°S). The tracer concentration between 10 and 50 years of simulation also remains the same in the drogued SIO accumulation region. In con-

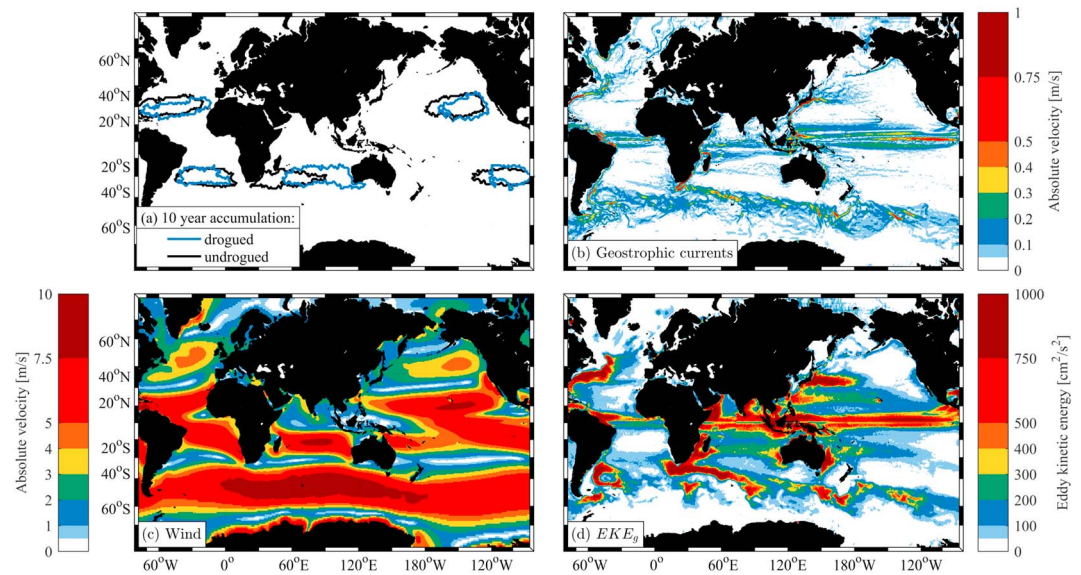


Figure 5. (a) Outlines of the spatial extent of the simulated subtropical accumulation regions after 10 years using transport matrices derived from drogued and undrogued drifter locations (black lines in Figures 3e and 3h, respectively). Global mean (b) geostrophic currents, based on GlobCurrent-v3 1993–2015 data; (c) wind, based on European Centre for Medium-Range Weather Forecasts ERA-Interim Reanalysis 1993–2015 data; and (d) geostrophic component of the eddy kinetic energy (EKE_g) calculated using geostrophic current anomalies based on GlobCurrent-v3 data.

trast, after 10 years the SIO subtropical accumulation region in the undrogued simulation (“undrogued SIO accumulation”) has a relatively low tracer concentration and is centered toward the west of the basin (Figure 3h; between 22–91°E and 24–39°S). After 50 years most of the tracer has depleted from the SIO and the undrogued SIO accumulation region no longer exists (Figure 3i). The two simulations have a weak statistically significant (anti)correlation in the SIO (Figure 4a).

The difference between the drogued and undrogued SIO accumulations is not only spatial but also temporal (Figure 4b). The amount of tracer in the drogued SIO accumulation quickly increases in the first 5 years of simulation. After 10 years, it remains stable at about 17% of the global available tracer, which is all of the tracer available in the IO. The amount of tracer in the undrogued SIO accumulation shows a very different evolution. It slowly increases to about 5% of the global available tracer in the first 5 years and then decreases, until after about 20 years no more tracer is left in the undrogued SIO accumulation region. Tracer from the undrogued SIO accumulation region possibly leaks into the South Atlantic subtropical accumulation region, we discuss this in more detail in section 4.

Several accumulation regions, other than the subtropical ones, are formed in the drogued and undrogued simulations as well. Because this paper focuses on the dynamics of the subtropical accumulations, we do not discuss these in detail, but for completeness we briefly mention them. In the undrogued simulation additional accumulation regions form in the Barents Sea, the Bay of Bengal, and along the east coast of Australia. As mentioned previously, the accumulation in the Barents Sea has been confirmed from plastic sampling studies (Cózar et al., 2017). High concentrations of plastics have also been sampled in the Bay of Bengal (Ryan, 2013). These plastics likely came from nearby sources, instead of accumulating in the Bay of Bengal over longer periods of time. Off the east coast of Australia high plastic concentrations, likely coming from both local and remote sources, have been sampled (Reisser et al., 2013). In the drogued simulation, a small accumulation region forms in the Mediterranean Sea. However, the Mediterranean Sea is relatively undersampled by the drifters, specifically by undrogued drifters, so we cannot rule out that this is a model artifact.

The differences between the drogued and undrogued simulations are due to the different mechanisms that transport the drogued and undrogued drifters. Our hypothesis is that these differences are especially pronounced in the SIO as a result of the unique dynamics of the SIO. To explain this further, we look at global oceanic and atmospheric dynamics.

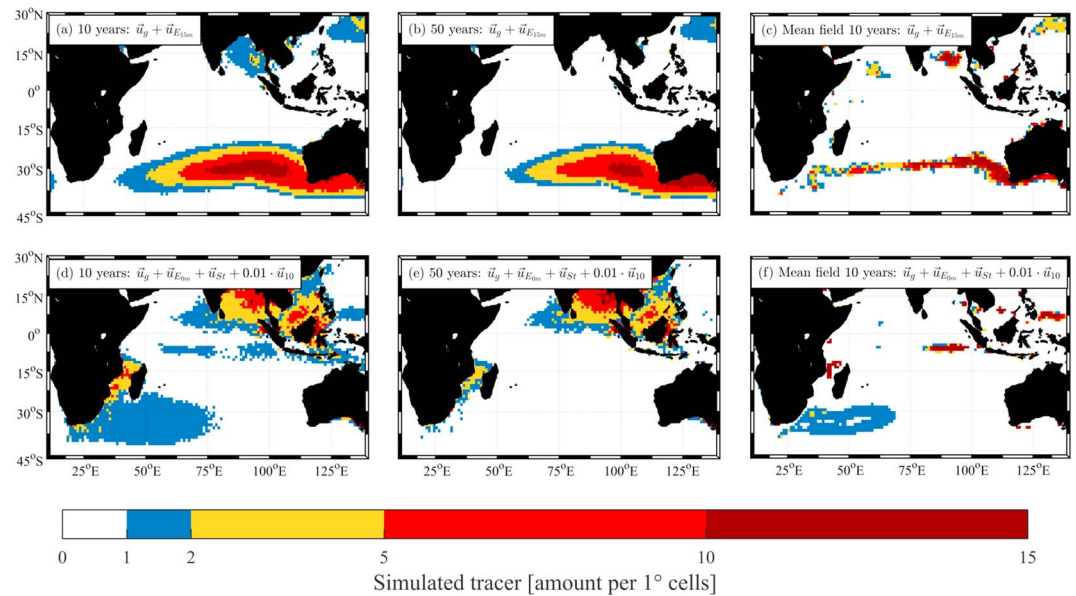


Figure 6. Simulated tracer density starting from a uniform initial condition, using transport matrices derived from virtual particle locations forced by (a, b) daily geostrophic currents and Ekman drift at 15-m depth from GlobCurrent-v3 1993–2015 data, $\bar{u}_g + \bar{u}_{E_{15m}}$; (d, e) daily geostrophic currents, surface Ekman drift, and Stokes drift from GlobCurrent-v3 1993–2015 data and 1% windage, calculated as 1% of the wind field at 10-m height based on European Centre for Medium-Range Weather Forecasts ERA-Interim Reanalysis 1993–2015 data, $\bar{u}_g + \bar{u}_{E_{0m}} + \bar{u}_{St} + 0.01 \cdot \bar{u}_{10}$; and (c, f) global mean fields as specified under (a, b) and (d, e) respectively. Simulation results after (a, c, d, f) 10 years and (b, e) 50 years are shown.

3.2. Oceanic and Atmospheric Dynamics

We consider global mean geostrophic currents (Figure 5b), associated eddy kinetic energy (EKE_g , Figure 5d), and the global mean wind field (Figure 5c) to explain the dynamics of the subtropical accumulation regions. The global mean wind field is related to both Stokes drift (through the generation of waves) and windage.

All subtropical accumulation regions in both the drogued and undrogued simulations (10-year outlines shown in Figure 5a for convenience) occur between 20°N (°S) and 40°N (°S). We expect accumulation to occur in these latitudes because of wind-driven Ekman convergence and downwelling. Other mechanisms may also influence the accumulation of buoyant debris through advection or dispersion. We expect drifters to disperse out of regions with high geostrophic current velocities or EKE_g . In the North and South Pacific Ocean, this is the case: The accumulation regions form toward the east of the Pacific basin, where geostrophic velocities and EKE_g are low. In the Atlantic Ocean, accumulation regions also occur outside regions with high geostrophic velocities and EKE_g . The accumulation regions in the SIO however, behave differently.

The SICC flows eastward between 22°S and 30°S (Figure 5b; Wijeratne et al., 2018; Menezes et al., 2014), through the northern part of the drogued SIO accumulation region. When the SICC reaches the coast of Western Australia, it feeds into the Leeuwin Current (LC; Lambert et al., 2016). The LC flows poleward, wrapping around the southern Australian coastline (geostrophic current velocities in light blue in Figure 5b, also seen in yellow EKE_g in Figure 5d; Pattiaratchi & Woo, 2009; Yit Sen Bull & van Sebille, 2016). We see this same feature in the outline of the drogued SIO accumulation region (Figure 5a). Our hypothesis is therefore that, in addition to Ekman currents, the dynamics of the drogued SIO accumulation are related to the geostrophic SICC and LC. Both the SICC and the LC are associated with high EKE_g (Figure 5d), but, unlike in the Pacific and Atlantic oceans, this apparently does not prevent the accumulation of buoyant debris.

Besides Ekman and geostrophic currents, we expect that the undrogued drifters are also influenced by Stokes drift and windage. The undrogued SIO accumulation region is centered uniquely toward the western side of the ocean basin, which is likely a result of the SIO wind field. There are two possible explanations for this.

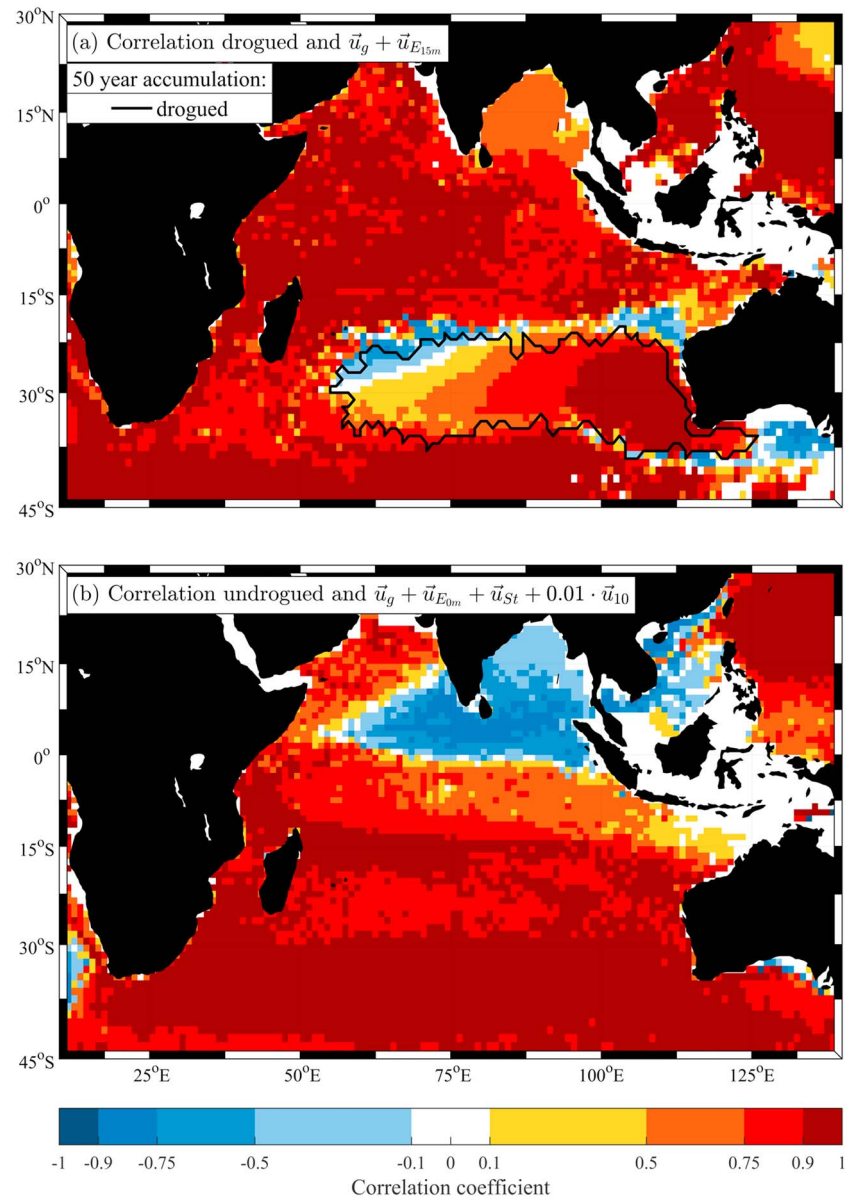


Figure 7. Point-wise linear Pearson correlation coefficient in each grid cell calculated over a simulation time of 50 years (i.e., 300 two-month values) between transport matrix simulations based on (a) drogued drifter locations and virtual particle locations forced by daily geostrophic currents and Ekman drift at 15-m depth, $\vec{u}_g + \vec{u}_{E_{15m}}$; (b) undrogued drifter locations and virtual particle locations forced by daily geostrophic currents, Ekman surface drift, Stokes drift, and 1% windage, $\vec{u}_g + \vec{u}_{E_{0m}} + \vec{u}_{St} + 0.01 \cdot \vec{u}_{10}$. A correlation value of 1 indicates perfect correlation; -1 indicates perfect anticorrelation. Correlations that are not statistically significant (within a confidence interval of 95%) are omitted (in white). The outline in black in (a) indicates the spatial extent of the simulated subtropical accumulation region after 50 years using the transport matrix based on drogued drifter locations (black line in Figures 3f). After 50 years the accumulation region using the transport matrix based on undrogued drifter locations has disappeared (Figure 3i), so no outline is shown in (b).

First, the Asian monsoon originates in the SIO where it affects the wind field (Joseph & Sijikumar, 2004; Findlater, 1969). The velocity of the easterly trade winds increases during the southwest monsoon season (e.g., Schott & McCreary, 2001). This leads to higher mean velocities of the trade winds in the SIO than in the (South) Pacific and Atlantic oceans (dark red area between approximately 60–90°E and 15–20°S in Figure 5c). The undrogued SIO accumulation region may center toward the western side of the basin because of these increased easterly winds.

Second, the geography of the western SIO boundary region is unique: the southern boundary of the African continent extends until roughly 35°S, whereas the region of low wind speed extends until roughly 40°S (Gordon, 2003). Because of this, the region of low wind speed extends past the southern tip of the African continent (Figure 5c). This may result in the undrogued SIO accumulation region extending southward of the African continent as well.

To summarize, our hypothesis is that the dynamics of the drogued SIO accumulation region are a result of 15-m depth Ekman $\vec{u}_{E_{15m}}$ and geostrophic currents \vec{u}_g , where we expect that the SICC and LC result in the accumulation region spanning almost the entire basin width. We expect that the dynamics of the undrogued SIO accumulation region are a result of surface Ekman $\vec{u}_{E_{0m}}$ and geostrophic currents \vec{u}_g but also Stokes drift \vec{u}_{St} and windage, $0.01 \cdot \vec{u}_{10}$. We hypothesize that Stokes drift and windage result in the accumulation region centering toward the west of the basin, due both to the strong mean easterly trade winds and the geography of the western boundary region. To confirm this, we run additional particle tracking simulations.

3.3. Particle Tracking Simulations

We run two simulations in the IO, forced by $\vec{u}_g + \vec{u}_{E_{15m}}$ (which likely represents the flow field of drogued drifters) and $\vec{u}_g + \vec{u}_{E_{0m}} + \vec{u}_{St} + 0.01 \cdot \vec{u}_{10}$ (which likely represents the flow field of undrogued drifters), for a period of 50 years and starting from a uniform initial condition. We use temporally varying forcing fields in these simulations. In addition, we run simulations with global mean forcing fields, to confirm our hypothesis that the dynamics of the drogued and undrogued SIO accumulation regions can largely be explained by persistent, mean oceanic, and atmospheric features of the SIO. In other words, we remove temporal variations from the forcing fields because we want to determine the influence of the predominant SIO dynamics on the accumulation of buoyant debris.

In the temporally varying $\vec{u}_g + \vec{u}_{E_{15m}}$ simulation, an accumulation region centered toward the east forms in the SIO spanning almost the entire basin width (Figures 6a and 6b). This simulation has a high statistically significant correlation with the drogued simulation (Figure 7a). In the global mean $\vec{u}_g + \vec{u}_{E_{15m}}$ simulation, an accumulation region spanning almost the entire basin width forms as well (Figure 6c). This is again similar to the drogued SIO accumulation, except that it is much more confined meridionally.

In the temporally varying $\vec{u}_g + \vec{u}_{E_{0m}} + \vec{u}_{St} + 0.01 \cdot \vec{u}_{10}$ simulation, an accumulation region with low tracer concentrations centered toward the western side of the basin forms (Figure 6d) and fully disappears after 50 years of simulation (Figure 6e). This simulation has a high statistically significant correlation with the undrogued simulation (Figure 7b). In addition to the subtropical accumulation region in the SIO, an accumulation forms in the Bay of Bengal as well, similar to, but more extensive than, in the undrogued simulation. In the global mean $\vec{u}_g + \vec{u}_{E_{0m}} + \vec{u}_{St} + 0.01 \cdot \vec{u}_{10}$ simulation, an accumulation region with low tracer concentration centered toward the west also forms, similar to the SIO undrogued accumulation region but more spatially confined.

These simulation results using temporally varying forcing fields confirm the drogued and undrogued drifter transport matrix simulations. In addition, the simulation results using global mean forcing fields confirm our hypothesis that the dynamics of the drogued and undrogued subtropical SIO accumulation regions are a result of persistent features of the IO.

4. Discussion

The aim of this paper is to determine the influence of different transport mechanisms on the dynamics of the subtropical accumulation regions. We used transport matrices based on observed locations from drogued and undrogued drifters to do this (drogued simulation and undrogued simulation, respectively). Drogued drifters are transported by ocean currents at a nominal 15-m depth, whereas undrogued drifters are transported by ocean currents in the uppermost surface layer as well as Stokes drift and windage. Intuitively it is easy to understand that there is a difference between the transport of the two types of drifters. However, the long-term and large-scale effect of different transport mechanisms on buoyant objects has not previously been shown. Maximenko et al. (2012) noted that drogued and undrogued drifters accumulate in the same regions, suggesting a remarkable (counterintuitive) robustness of the subtropical accumulation regions. In our simulation results, we see this robustness in the Pacific and Atlantic oceans. The subtropical accumulation region in the SIO, however, is very sensitive to different transport mechanisms.

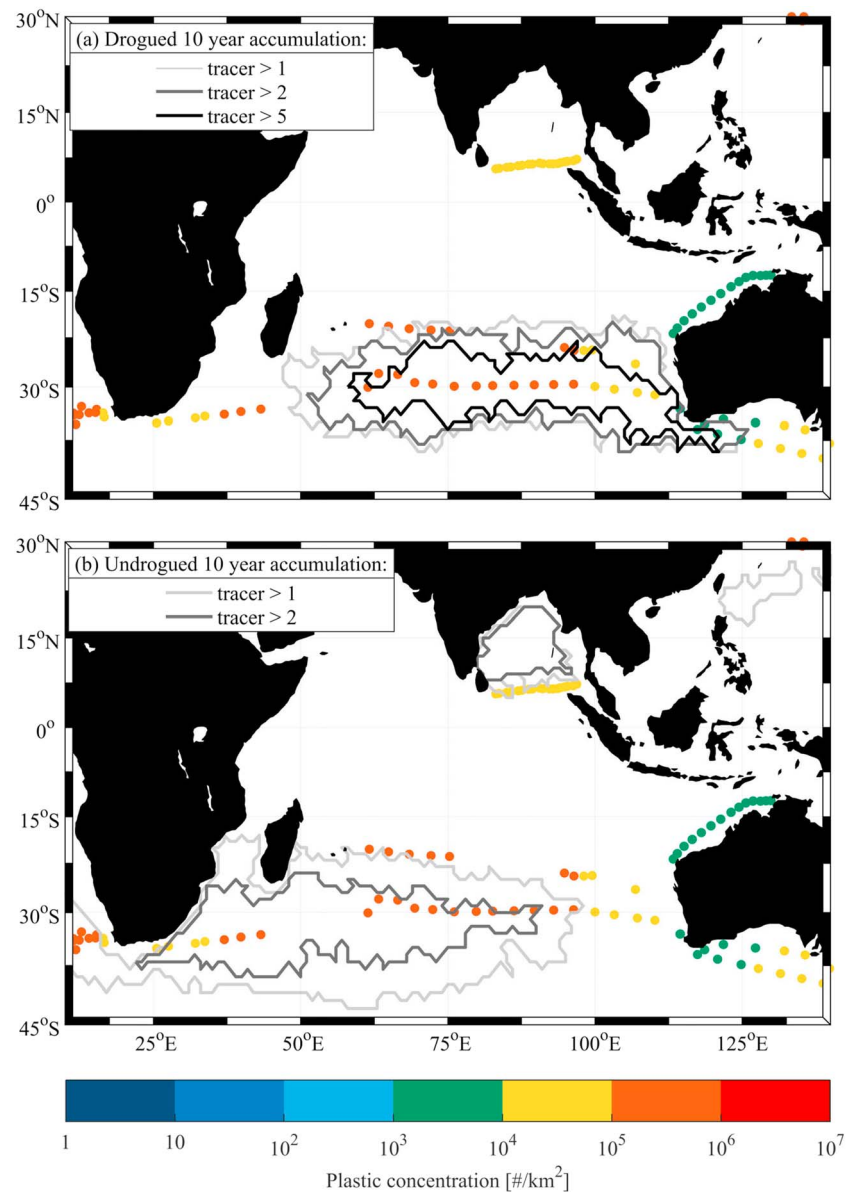


Figure 8. Standardized measurements of “small” (< 200-mm) buoyant plastics in the Indian Ocean. Measurements were standardized by van Sebille et al. (2015). Original sampling studies were performed by Morris (1980), Reisser et al. (2013), Eriksen et al. (2014), and Cózar et al. (2014). Outlines indicate the simulated Indian Ocean subtropical and Bay of Bengal accumulation regions after 10 years of simulation using transport matrices based on (a) drogued drifter locations and (b) undrogued drifter locations. The accumulation regions are defined as regions with at least 50 adjacent grid cells where the tracer concentration exceeds 1, 2, or 5 per $1 \times 1^\circ$ cell. Note that in panel b no accumulation region with a tracer concentration > 5 per $1 \times 1^\circ$ occurs.

In the drogued simulation, a persistent, large-scale subtropical accumulation region forms in the SIO that spans almost the entire basin width. In the undrogued simulation an accumulation with relatively low tracer concentrations forms on the western side of the SIO basin. This accumulation region is highly dispersive and disappears completely after 20 years of simulation.

We propose that the sensitivity of the subtropical SIO accumulation region to different transport mechanisms is due to the unique oceanic and atmospheric dynamics of the SIO, specifically, due to (1) the SICC that flows eastward through the center of the subtropical SIO gyre, which likely results in the drogued SIO accumulation region spanning almost the entire basin width; (2) the unique poleward flowing Leeuwin Current at the eastern boundary of the SIO gyre, which likely results in the drogued SIO accumulation region wrapping around the southern Australian coastline; (3) the strong easterly trade winds in the SIO that are a

result of the Asian monsoon system, which likely results in the undrogued SIO accumulation region centering toward the western side of the basin; and (4) the unique geography at the western boundary of the SIO gyre that provides a connection between the SIO and the South Atlantic Ocean, which likely results in leakage of tracer from the undrogued SIO accumulation region into the South Atlantic. Additional simulations with global mean forcing fields confirm that persistent SIO features are likely responsible for the dynamics of the subtropical SIO accumulation regions.

Because we are interested in the dynamics of accumulation regions, our simulations start with tracer spread uniformly across the global oceans. This allows us to analyze the behavior of buoyant debris, independent of the distribution of sources. However, this does raise the question how our results would be influenced if we include plastic sources instead of using a uniform initial condition. Most coastal (Jambeck et al., 2015) and riverine (Lebreton et al., 2017; Schmidt et al., 2017) sources of plastics are estimated to enter the northern IO, with only a few sources entering into the SIO. Buoyant debris does not tend to cross the equator (Maximenko et al., 2012), so the amount of plastic that is available to accumulate in the subtropical SIO is probably limited. This would reinforce our result from the undrogued simulation, which indicates low surface tracer concentrations in the subtropical SIO.

Ideally, we would like to confirm our simulation results and conclusions with measurements. Unfortunately, the sampling studies in the IO are too scarce to draw any definitive conclusions. Comparing the accumulation regions after 10 years in the drogued and undrogued simulations with sampled plastic concentrations is inconclusive (Figures 8a and 8b). Both simulated subtropical SIO accumulation regions overlap with several locations where high plastic concentrations ($> 10^5$ [#/ km^2]) were measured. However, they also fail to capture several other locations.

Our results indicate that it is important to take different transport mechanisms into account when studying drifting objects. For this to be useful in particle tracking studies, we need to understand exactly which mechanisms are relevant. In our simulations using temporally varying and global mean forcing fields, we made a first step toward this. We used a simplified linear velocity parametrization to take Stokes drift and windage into account, which is commonly used (Abascal et al., 2009; Breivik & Allen, 2008; Rohrs et al., 2012). Although this is sufficient for a first-order approximation and for the purposes of this paper, it unlikely captures the complex, time-varying dynamics of an individual item of drifting buoyant debris.

We used the drogued and undrogued drifters as a proxy for buoyant plastic debris (plastics). It is unclear how plastics relate to the drifters. Depending on their rising velocity, and wind and wave conditions (Brunner et al., 2015; Kukulka & Brunner, 2015; Kukulka et al., 2012), plastics drift both on the sea surface and submerged in the upper ocean (Kooi et al., 2016; Reisser et al., 2015). As a result, both types of drifters are possible valid proxies. However, we need a more extensive data set of the material properties of plastics (shape, size, density) before we can relate them to drifters. Because most open-ocean studies, with the exception of the recent study by Lebreton et al. (2018), focus on so-called “microplastics,” this is especially true for larger plastic items.

We also need to relate material properties of plastics to usable transport properties, such as windage coefficient or rising velocity. Several studies have reported a correlation between the size of plastics and their rising velocity (Kooi et al., 2016; Lebreton et al., 2018; Reisser et al., 2015). Chubarenko et al. (2016) determined the windage coefficient of plastics based on size and density, and Lebreton et al. (2018) derived a windage coefficient for plastics in the North Pacific garbage patch by using it as a calibration parameter for their numerical model. Despite these efforts there is no generally applicable method to relate material properties to relevant transport properties of plastics.

Our results lead to several implications and questions for follow-up research. First, the undrogued simulations show that the subtropical SIO accumulation region disappears within 20 years. A relevant question is where buoyant debris ends up. A reasonable hypothesis is that debris from the SIO moves into the South Atlantic Ocean. Interaction between these two accumulation regions has already been shown (van Sebille et al., 2012), but it still needs to be confirmed if this is enough to explain the emptying of the subtropical SIO accumulation region. Second, the drogued simulations show a persistent accumulation forming in a region that is associated with high eddy kinetic energy (Dilmahamod et al., 2018). It is not yet clear why this accumulation is so stable. Third, large amounts of plastics are estimated to enter the northern IO (Jambeck et al., 2015; Lebreton et al., 2017; Schmidt et al., 2017). If these plastics do not accumulate in the subtropics

(because there is no northern IO subtropical gyre and buoyant debris is unlikely to cross the equator), an important question is what does happen to these plastics.

Finally, our results from the drogued and undrogued simulations may explain previous inconsistent model results in the SIO. Studies that find high concentrations of buoyant debris toward the western side of the subtropical SIO (Maximenko et al., 2012; van Sebille et al., 2012) are all based on drifter transport matrices (from combined drogued and undrogued drifters). Studies that find high concentrations in the center and toward the east of the SIO all use particle tracking models forced by ocean surface currents from either satellite products (Kubota et al., 2005) or ocean general circulation models (Lebreton et al., 2012; Maes et al., 2018). Maes et al. (2018) proposed that the differences between these results are due to a lack of observed drifter locations in the IO. Instead, we propose that the differences are a result of including undrogued drifters in the transport matrices used by Maximenko et al. (2012) and van Sebille et al. (2012). Because of this, surface transport mechanisms such as windage and Stokes drift, as well as a different direction of the Ekman currents at the surface and at a nominal 15-m depth, are included in these simulations. These transport mechanisms are not included in the particle tracking methods. The latter simulations therefore agree better with our drogued simulations.

5. Conclusions

We examined the influence of different transport mechanisms on the dynamics of the subtropical accumulation region in the IO using transport matrices based on observed locations from drogued and undrogued drifters. Our results indicate that accumulation of buoyant debris in the subtropical SIO is very sensitive to different transport mechanisms. The unique oceanic and atmospheric dynamics of the SIO have a significant influence on this sensitivity.

Buoyant debris transported by ocean surface currents at a nominal 15-m depth accumulates in high concentrations in the subtropical SIO in a region that spans almost the entire width of the SIO basin and wraps around the southern coastline of Australia. This is most likely due to the SICC that flows eastward through the subtropical gyre, and the Leeuwin Current that flows poleward along the western Australian coastline.

In contrast, buoyant debris transported by surface dynamics (ocean surface currents between 0- and 1-m depth, Stokes drift, and windage) concentrates in a highly dispersive region toward the west of the subtropical SIO. This is most likely due to the strong easterly trade winds in the SIO as well as the unique geography at the western boundary of the SIO gyre, which provides a connection between the SIO and the South Atlantic Ocean.

Acknowledgments

Global drifter trajectory data are available from the NOAA Global Drifter Program (www.aoml.noaa.gov/phod/dac). Surface geostrophic, Stokes drift, surface Ekman, and Ekman 15-m depth velocity fields are products of the GlobCurrent project (www.globcurrent.org). Wind fields from the ERA-Interim Reanalysis data set are available from ECMWF (apps.ecmwf.int/datasets/data/interim-full-moda). Our code to construct and run drifter transport matrix simulations is available under an MIT license (www.github.com/mheen/gdp_tm). M. v. d. M. was supported by an Australian Government Research Training Program (RTP) Scholarship and a CFH & EA Jenkins Postgraduate Research Scholarship at the University of Western Australia. E. v. S. was supported by the European Research Council (ERC) under the European Union's Horizon 2020 research and innovation program (grant agreement 715386). Comments from two anonymous reviewers helped to improve this manuscript.

References

- Abascal, A., Castanedo, S., Mendez, F., Medina, R., & Losada, I. (2009). Calibration of a Lagrangian transport model using drifting buoys deployed during the Prestige oil spill. *Journal of Coastal Research*, 25, 80–90.
- Barnes, D., Walters, A., & Goncalves, L. (2010). Macroplastics at sea around Antarctica. *Marine Environmental Research*, 70, 250–252.
- Beal, L., de Ruijter, W., Biastoch, A., & Zahn, R. (2011). On the role of the Agulhas system in ocean circulation and climate. *Nature*, 472, 429–436. <https://doi.org/10.1038/nature09983>
- Beron-Vera, F., Olascoaga, M., & Lumpkin, R. (2016). Inertia-induced accumulation of flotsam in the subtropical gyres. *Geophysical Research Letters*, 43, 12,228–12,233. <https://doi.org/10.1002/2016GL071443>
- Breivik, O., & Allen, A. (2008). An operational search and rescue model for the Norwegian Sea and the North Sea. *Journal of Marine Systems*, 69, 99–113.
- Breivik, O., Allen, A., Maisondieu, C., & Roth, J. (2011). Wind-induced drift of objects at sea: The leeway field method. *Applied Ocean Research*, 33, 100–109. <https://doi.org/10.1016/j.apor.2011.01.005>
- Brunner, K., Kukulka, T., Proskurovski, G., & Law, K. (2015). Passive buoyant tracers in the ocean surface boundary layer: 2. Observations and simulations of microplastic marine debris. *Journal of Geophysical Research: Oceans*, 120, 7559–7573. <https://doi.org/10.1002/2015JC010840>
- Chubarenko, I., Bagaev, A., Zobkov, M., & Esiukova, E. (2016). On some physical and dynamical properties of microplastic particles in the marine environment. *Marine Pollution Bulletin*, 108, 105–112.
- Cózar, A., Marti, E., Duarte, C., de Lomas, J. G., van Sebille, E., Ballatore, T., et al. (2017). The Arctic Ocean as a dead end for floating plastics in the North Atlantic branch of the thermohaline circulation. *Science Advances*, 3, e1600582. <https://doi.org/10.1126/sciadv.1600582>
- Cózar, A., Echevarria, F., Gonzalez-Gordillo, J., Irigoien, X., Ubeda, B., Hernandez-Leon, S., et al. (2014). Plastic debris in the open ocean. *PNAS*, 111, 10,239–10,244.
- Dee, D., Uppala, S., Simmons, A., Berrisford, P., Poli, P., Kobayashi, S., et al. (2011). The ERA-Interim reanalysis: Configuration and performance of the data assimilation system. *Quarterly Journal of the Royal Meteorological Society*, 137, 553–597. <https://doi.org/10.1002/qj.828>
- Dellnitz, M., Froyland, G., Horenkamp, C., Padberg-Gehle, K., & Gupta, A. S. (2009). Seasonal variability of the subpolar gyres in the Southern Ocean: A numerical investigation based on transfer operators. *Nonlinear Processes in Geophysics*, 16, 655–664.

- Dilmahamad, A., Aguiar-González, B., Penven, P., Reason, C., de Ruijter, W., Malan, N., & Hermes, J. (2018). SIDDIES corridor: A major east-west pathway of long-lived surface and subsurface eddies crossing the subtropical South Indian Ocean. *Journal of Geophysical Research: Oceans*, *123*, 5406–5425. <https://doi.org/10.1029/2018JC013828>
- Duhec, A., Jeanne, R., Maximenko, N., & Hafner, J. (2015). Composition and potential origin of marine debris stranded in the western Indian Ocean on remote Alphonse Island, Seychelles. *Marine Pollution Bulletin*, *96*, 76–86.
- Eriksen, M., Lebreton, L., Carson, H., Thiel, M., Moore, C., Borror, J., et al. (2014). Plastic pollution in the world's oceans: More than 5 trillion plastic pieces weighing over 250,000 tons afloat at sea. *PLOS ONE*, *9*, e111913. <https://doi.org/10.1371/journal.pone.0111913>
- Eriksen, M., Maximenko, N., Thiel, M., Cummins, A., Lattin, G., Wilson, S., et al. (2013). Plastic pollution in the South Pacific subtropical gyre. *Marine Pollution Bulletin*, *68*, 71–76.
- Findlater, J. (1969). A major low-level air current near the Indian Ocean during the northern summer. *Quarterly Journal of the Royal Meteorological Society*, *95*, 362–380. <https://doi.org/10.1002/qj.49709540409>
- Froyland, G., Stuart, R., & van Sebille, E. (2014). How well-connected is the surface of the global ocean? *Chaos*, *24*, 033126. <https://doi.org/10.1063/1.4892530>
- Gordon, A. (2003). The browniest retroflection. *Nature*, *421*, 904–905.
- Grodsky, S., Lumpkin, R., & Carton, J. (2011). Spurious trends in global surface drifter currents. *Geophysical Research Letters*, *38*, L10606. <https://doi.org/10.1029/2011GL047393>
- Hansen, D., & Poulain, P. (1996). Quality control and interpolations of WOCETOGA drifter data. *Journal of Atmospheric and Oceanic Technology*, *13*, 900–909.
- Jambeck, J., Geyer, R., Wilcox, C., Siegler, T., Perryman, M., Andrady, A., et al. (2015). Plastic waste inputs from land into the ocean. *Science*, *347*, 768–771.
- Jian, F., & Wu, L. (2011). Seasonal modulation of eddy kinetic energy and its formation mechanisms in the southeast Indian Ocean. *Journal of Physical Oceanography*, *41*, 657–665.
- Joseph, P., & Sijikumar, S. (2004). Intraseasonal variability of the low-level jetstream of the Asian summer monsoon. *Journal of Climate*, *17*, 1449–1458. <https://doi.org/10.1175/1520-0442>
- Khatiwala, S., Visbeck, M., & Cane, M. (2005). Accelerated simulation of passive tracers in ocean circulation models. *Ocean Modelling*, *9*, 51–69.
- Kooi, M., Reisser, J., Slat, B., Ferrari, F., Schmid, M., Cunsolo, S., et al. (2016). The effect of particle properties on the depth profile of buoyant plastics in the ocean. *Scientific Reports*, *6*, 33882. <https://doi.org/10.1038/srep33882>
- Kubota, M. (1994). A mechanism for the accumulation of floating marine debris north of Hawaii. *Journal of Physical Oceanography*, *24*, 1059–1064.
- Kubota, M., Takayama, K., & Namimoto, D. (2005). Pleading for the use of biodegradable polymers in favor of marine environments and to avoid an asbestos-like problem for the future. *Applied Microbiological Biotechnology*, *67*, 469–476.
- Kukulka, T., & Brunner, K. (2015). Passive buoyant tracers in the ocean surface boundary layer: 1. Influence of equilibrium wind-waves on vertical distributions. *Journal of Geophysical Research: Oceans*, *120*, 3837–3858. <https://doi.org/10.1002/2014JC010487>
- Kukulka, T., Proskurovski, G., Moret-Ferguson, S., Meyer, D., & Law, K. (2012). The effect of wind mixing on the vertical distribution of buoyant plastic debris. *Geophysical Research Letters*, *39*, L07601. <https://doi.org/10.1029/2012GL051116>
- Lambert, E., Bars, D. L., & de Ruijter, W. (2016). The connection of the Indonesian Throughflow, South Indian Ocean Countercurrent and the Leeuwin Current. *Ocean Science*, *12*, 771–780. <https://doi.org/10.5194/os-12-771-2016>
- Lange, M., & van Sebille, E. (2017). Parcels v0.9: Prototyping a Lagrangian ocean analysis framework for the petascale age. *Geoscientific Model Development*, *10*, 4175–4186. <https://doi.org/10.50194/gmd-10-4175-2017>
- Lavers, J., & Bond, A. (2017). Exceptional and rapid accumulation of anthropogenic debris on one of the world's most remote and pristine islands. *PNAS*, *114*, 6052–6055. <https://doi.org/10.1073/pnas.1619818114>
- Law, K. (2017). Plastics in the marine environment. *Annual Review of Marine Science*, *9*, 205–229.
- Lebreton, L., Greer, S., & Borrero, J. (2012). Numerical modelling of floating debris in the world's oceans. *Marine Pollution Bulletin*, *64*, 653–661. <https://doi.org/10.1016/j.marpolbul.2011.10.027>
- Lebreton, L., Slat, B., Ferrari, F., Sainte-Rose, B., Aitken, J., Marthouse, R., et al. (2018). Evidence that the Great Pacific Garbage Patch is rapidly accumulating plastic. *Scientific Reports*, *8*, 4666. <https://doi.org/10.1038/s41598-018-22939-w>
- Lebreton, L., van der Zwet, J., Damsteeg, J., Slat, B., Andrady, A., & Reisser, J. (2017). River plastic emissions to the world's oceans. *Nature Communications*, *8*, 15611. <https://doi.org/10.1038/ncomms15611>
- Lumpkin, R., Centurioni, L., & Perez, R. C. (2016). Fulfilling observing system implementation requirements with the global drifter array. *Journal of Atmospheric and Oceanic Technology*, *33*, 685–695. <https://doi.org/10.1175/JTECH-D-15-0255.1>
- Lumpkin, R., Grodsky, S., Centurioni, L., Rio, M., Carton, J., & Lee, D. (2013). Removing spurious low-frequency variability in drifter velocities. *Journal of Atmospheric and Oceanic Technology*, *30*, 353–360. <https://doi.org/10.1175/JTECH-D-12-00139.1>
- Lumpkin, R., & Pazos, M. (2007). Measuring surface currents with surface velocity program drifters: The instrument, its data and some recent results. In A. Mariano, T. Rossby, & D. Kirwan (Eds.), *Lagrangian analysis and prediction of coastal and ocean dynamics* (pp. 39–67). Cambridge: Cambridge University Press.
- Lutjeharms, J. (2006). The Agulhas Current retroflection, *The Agulhas Current*. Würzburg, Germany: Springer.
- Maes, C., Grima, N., Blanke, B., Martinez, E., Paviet-Salomon, T., & Huck, T. (2018). A surface superconvergence pathway connecting the South Indian Ocean to the subtropical South Pacific gyre. *Geophysical Research Letters*, *45*, 1915–1922. <https://doi.org/10.1002/2017GL076366>
- Martinez, E., Maamaatuaiahutapu, K., & Taillandier, V. (2009). Floating marine debris surface drift: Convergence and accumulation toward the South Pacific subtropical gyre. *Marine Pollution Bulletin*, *58*, 1347–1355.
- Maximenko, N., Hafner, J., & Niiler, P. (2012). Pathways of marine debris derived from trajectories of Lagrangian drifters. *Marine Pollution Bulletin*, *65*, 51–62. <https://doi.org/10.1016/j.marpolbul.2011.04.016>
- Maximenko, N., Niiler, P., Rio, M., Melnichenko, O., Centurioni, L., Chambers, D., et al. (2009). Mean dynamic topography of the ocean derived from satellite and drifting buoy data using three different techniques. *Journal of Atmospheric and Oceanic Technology*, *26*, 1910–1919. <https://doi.org/10.1175/2009JTECHO672.1>
- McAdam, R., & van Sebille, E. (2018). Surface connectivity and interocean exchanges from drifter-based transition matrices. *Journal of Geophysical Research: Oceans*, *123*, 514–532. <https://doi.org/10.1002/2017JC013363>
- Menezes, V., Phillips, H., Schiller, A., Bindoff, N., Domingues, C., & Vianna, M. (2014). South Indian Countercurrent and associated fronts. *Journal of Geophysical Research: Oceans*, *119*, 6763–6791. <https://doi.org/10.1002/2014JC010076>
- Miron, P., Beron-Vera, F., Olascoaga, M., Froyland, G., Pérez-Brunius, P., & Sheinbaum, J. (2019). Lagrangian geography of the deep Gulf of Mexico. *Journal of Physical Oceanography*, *49*, 269–290. <https://doi.org/10.1175/JPO-D-18-0073.1>

- Moore, C., Moore, S., Leecaster, M., & Weisberg, S. (2001). A comparison of plastic and plankton in the North Pacific central gyre. *Marine Pollution Bulletin*, *42*, 1297–1300.
- Morris, R. (1980). Plastic debris in the surface waters of the South Atlantic. *Marine Pollution Bulletin*, *11*, 164–166.
- Niiler, P., Sybrandy, A., Bi, K., Poulain, P., & Bitterman, D. (1995). Measurements of the water-following capability of holey-sock and tristar drifters. *Deep Sea Research I*, *42*, 1950–1964.
- Palastanga, V., van Leeuwen, P., Schouten, M., & de Ruijter, W. (2007). Flow structure variability in the subtropical Indian Ocean: Instability of the South Indian Ocean Countercurrent. *Journal of Geophysical Research*, *112*, C01001. <https://doi.org/10.1029/2005JC003395>
- Pattiaratchi, C., & Woo, M. (2009). The mean state of the Leeuwin Current system between North West Cape and Cape Leeuwin. *Journal of the Royal Society of Western Australia*, *92*, 221–241.
- Poulain, P., Gerin, R., & Mauri, E. (2009). Wind effects on drogued and undrogued drifters in the eastern Mediterranean. *Journal of Atmospheric and Oceanic Technology*, *26*, 1144–1156.
- Reisser, J., Shaw, J., Wilcox, C., Hardesty, B., Proietti, M., Thums, M., & Pattiaratchi, C. (2013). Marine plastic pollution in waters around Australia: Characteristics, concentrations, and pathways. *PLoS ONE*, *8*, e80466. <https://doi.org/10.1371/journal.pone.0080466>
- Reisser, J., Slat, B., Noble, K., du Plessis, K., Epp, M., Proietti, M., et al. (2015). The vertical distribution of buoyant plastics at sea: An observational study in the North Atlantic gyre. *Biogeosciences*, *12*, 1249–1256.
- Rio, M., Mulet, S., & Picot, N. (2014). Beyond GOCE for the ocean circulation estimate: Synergetic use of altimetry, gravimetry and in situ data provides new insight into geostrophic and Ekman currents. *Geophysical Research Letters*, *41*, 8918–8925. <https://doi.org/10.1002/2014GL061773>
- Rohrs, J., Christensen, K., Hole, L., Brostrom, G., Drivdal, M., & Sundby, S. (2012). Observation-based evaluation of surface wave effects on currents and trajectory forecasts. *Ocean Dynamics*, *62*, 1519–1533.
- Ryan, P. (2013). A simple technique for counting marine debris at sea reveals steep litter gradients between the Straits of Malacca and the Bay of Bengal. *Marine Pollution Bulletin*, *69*, 128–136.
- Schmidt, C., Krauth, T., & Wagner, S. (2017). Export of plastic debris by rivers into the sea. *Environmental Science and Technology*, *51*, 12,246–12,253. <https://doi.org/10.1021/acs.est.7b02368>
- Schott, F., & McCreary, J. (2001). The monsoon circulation of the Indian Ocean. *Progress in Oceanography*, *51*, 1–123.
- Schott, F., Xie, S., & McCreary, J. (2009). Indian Ocean circulation and climate variability. *Reviews of Geophysics*, *47*, RG1002. <https://doi.org/10.1029/2007RG000245>
- Ser-Giacomi, E., Rossi, V., Lopez, C., & Hernandez-Garcia, E. (2015). Flow networks: A characterization of geophysical fluid transport. *Chaos*, *25*, 036404. <https://doi.org/10.1063/1.4908231>
- Sherman, P., & van Sebille, E. (2016). Modeling marine surface microplastic transport to assess optimal removal locations. *Environmental Research Letters*, *11*, 1–6. <https://doi.org/10.1088/1748-9326/11/1/014006>
- Stramma, L., & Lutjeharms, J. (1997). The flow field of the subtropical gyre of the South Indian Ocean. *Journal of Geophysical Research*, *102*, 5513–5530.
- van Sebille, E., England, M., & Froyland, G. (2012). Origin, dynamics and evolution of ocean garbage patches from observed surface drifters. *Environmental Research Letters*, *7*, 044040. <https://doi.org/10.1088/1748-9326/7/4/044040>
- van Sebille, E., Wilcox, C., Lebreton, L., Maximenko, N., Hardesty, B., van Franeker, J., et al. (2015). A global inventory of small floating plastic debris. *Environmental Research Letters*, *10*, 124006. <https://doi.org/10.1088/1748-9326/10/12/124006>
- Wijeratne, S., Pattiaratchi, C., & Proctor, R. (2018). Estimates of surface and subsurface boundary current transport around Australia. *Journal of Geophysical Research: Oceans*, *123*, 3444–3466. <https://doi.org/10.1029/2017JC013221>
- Wolter, K., & Timlin, M. (1993). Monitoring ENSO in COADS with a seasonally adjusted principal component index. *Proceedings of the 17th Climate Diagnostics Workshop*, 52–57. Norman, OK
- Wolter, K., & Timlin, M. (1998). Measuring the strength of ENSO events—How does 1997/98 rank? *Weather*, *53*, 315–324.
- Yit Sen Bull, C., & van Sebille, E. (2016). Sources, fate, and pathways of Leeuwin Current water in the Indian Ocean and Great Australian Bight: A Lagrangian study in an eddy-resolving ocean model. *Journal of Geophysical Research: Oceans*, *121*, 1626–1639. <https://doi.org/10.1002/2015JC011486>